AIMS Geosciences

AIMS Geosciences, 12(4): 1061–1086.
DOI: 10.3934/geosci.2026041
Received: 09 August 2026
Revised: 12 September 2026
Accepted: 08 October 2026
Published: 16 November 2026

https://www.aimspress.com/journal/geosciences

Research article

Digital mapping of SPT-derived Vs30 for magnitude- and period-dependent seismic amplification in urban alluvial soils

Şahin Çağlar Tuna*

Department of Civil Engineering, Yaşar University, Izmir, Turkey

* **Correspondence:** Email: caglar.tuna@yasar.edu.tr; Tel: +90 (232) 570 7070.

Abstract: Digital soil mapping can convert irregular borehole information into spatially continuous engineering ground models, but many applications remain focused on soil classification or interpolated index properties. This study developed a framework that transforms depth-resolved standard penetration test profiles into a spatial Vs30 proxy field and couples this field with observed strong-motion behavior. An ensemble of SPT–Vs correlations is used to derive borehole-scale shear-wave velocity profiles and corresponding Vs30 proxies. Strong-motion records are independently analyzed to isolate site-dependent components of PGA and spectral acceleration after accounting for event and path effects. The resulting Vs30–amplification relationships are transferred to the digital soil field to generate magnitude- and period-dependent amplification layers, while uncertainties associated with the SPT transformation, spatial interpolation, and amplification model are propagated through the mapping procedure. The borehole-derived proxies reveal appreciable local variability across the alluvial deposits, whereas spatial validation indicates that the digital field captures broad stiffness patterns at the spatial scale supported by the borehole network. Stronger amplification is consistently associated with lower Vs30, but the modulation of this relationship varies across the response spectrum. Magnitude-associated effects remain pronounced for PGA and long-period response after explicit control for reference-rock input-motion intensity, whereas intermediate-period amplification shows stronger coupling to the corresponding spectral input-motion level. The same mapped soil field therefore acquires different engineering significance depending on earthquake magnitude, input-motion intensity, and spectral period. By treating the digital soil field as a spatial substrate whose seismic expression changes with spectral period and seismic scenario, the proposed framework extends

descriptive subsurface mapping toward observation-constrained, scenario-dependent interpretation of urban ground-motion variability.

Keywords: digital soil mapping; SPT; Vs30; seismic amplification; strong-motion records; alluvial soils; spatial variability

1. Introduction

Spatial characterization of near-surface ground conditions is a fundamental component of geotechnical earthquake engineering because local soil properties influence both the amplitude and frequency content of earthquake ground motions. Among the parameters used for this purpose, the time-averaged shear-wave velocity in the upper 30 m (Vs30) has become one of the most widely adopted proxies for seismic site condition, being extensively used in building-code site classification, ground-motion models, ShakeMap applications, and regional seismic-hazard assessments [1,2]. The widespread use of Vs30 reflects its ability to provide a compact representation of shallow stiffness, but it does not imply that near-surface conditions are spatially uniform or that a single Vs30-based site class uniquely determines seismic response. Observational studies have repeatedly shown substantial site-to-site variability in sedimentary settings, including frequency-dependent amplification patterns that cannot be represented adequately by a single scalar amplification coefficient [3,4].

Digital soil mapping provides a natural framework for representing this spatial variability. The general concept was formalized as the quantitative prediction of soil properties or classes from point observations and spatially exhaustive environmental information, using statistical, geostatistical, and machine-learning methods to transform sparse measurements into continuous spatial fields [5]. Although digital soil mapping originated primarily in soil science, the same conceptual framework has direct relevance to engineering-ground characterization, where boreholes, penetration tests, geophysical measurements, and geological information are inherently discrete, while engineering decisions require spatially distributed representations. Recent studies have consequently used Vs and Vs30 as mappable engineering attributes for seismic site characterization and regional hazard applications. For example, spatially explicit Vs30 models have been developed using geostatistical methods to characterize both the mapped values and their spatial correlation structure, which is relevant to spatially distributed seismic-hazard and infrastructure-risk assessment [6]. Likewise, studies integrating MASW measurements and borehole data have demonstrated that SPT-derived shear-wave velocity information can be used to extend seismic site characterization beyond the limited locations where direct geophysical measurements are available [7].

The standard penetration test (SPT) is particularly attractive in this context because large archives of borehole-based SPT data are available in many urban areas for which spatially dense Vs measurements do not exist. Empirical relations between penetration resistance and shear-wave velocity have therefore been investigated for several decades. Ohta and Goto [8] showed that SPT resistance, depth, geological age, and soil type can collectively explain a substantial proportion of measured Vs variability, while later regional studies have developed and evaluated alternative empirical relations

under different geological conditions. In Türkiye, Hasancebi and Ulusay [9] demonstrated that SPT blow count provides a significant predictor of shear-wave velocity and evaluated these relationships explicitly for ground-shaking assessment. Similar work has subsequently emphasized both the practical value and the regional dependence of SPT–Vs correlations, including applications in alluvial deposits and seismic site classification [7,10]. Because empirical Vs estimates inevitably inherit model uncertainty, the use of multiple correlations rather than a single deterministic transformation provides a more transparent basis for deriving Vs30 from borehole profiles. The treatment of boreholes shallower than 30 m is also important. Previous studies have shown that profile extrapolation can materially affect estimated Vs30, and bottom-constant extrapolation has been evaluated as one practical solution where direct measurements do not extend to the full 30 m depth [11].

Translating a mapped Vs30 field into seismic engineering information introduces an additional level of complexity. Modern ground-motion models generally describe site response as a function of Vs30, while also allowing the response to depend on ground-motion amplitude and spectral period. The NGA-West2 framework, for example, incorporates Vs30-dependent site terms and nonlinear site response into the prediction of PGA and response spectra [2,12]. Seyhan and Stewart [13] used NGA-West2 observations and simulations to show that site amplification varies systematically with Vs30, with nonlinear behavior becoming important for relatively soft sites and the strength of Vs30 scaling varying with spectral period. More generally, studies of weak and strong ground motions have shown that the seismic response of soil profiles cannot always be characterized by Vs30 alone, particularly where profile shape, fundamental frequency, deeper velocity structure, or impedance contrasts become important [14]. Observational studies in sedimentary basins similarly demonstrate that regional and basin effects can produce large frequency-dependent departures from predictions based solely on shallow site proxies.

These considerations suggest that the engineering interpretation of a digital soil map should not terminate with the mapped geotechnical parameter itself. A spatial Vs30 field represents the distribution of shallow ground stiffness, whereas its seismic consequence depends on how that stiffness interacts with the spectral content and intensity of earthquake shaking. Recent strong-motion analyses in Türkiye have demonstrated systematic relationships between Vs30 and observed site amplification, with pronounced frequency dependence and stronger low-frequency amplification in sedimentary settings [15]. At the same time, empirical and semi-empirical site-response models indicate that amplification cannot generally be represented as a fixed multiplier independent of the characteristics of the input motion [13]. This creates an opportunity to extend digital soil mapping from a descriptive representation of subsurface properties toward a response-oriented spatial model in which the same mapped soil field may acquire different engineering significance under different earthquake and spectral conditions.

In this study, depth-resolved SPT profiles from an urban alluvial area are transformed into empirical Vs profiles using an ensemble of established SPT–Vs relationships and subsequently integrated to construct a digital Vs30 proxy field. The treatment of incomplete 30-m profiles is evaluated through masked validation, while the spatial field is assessed using location-independent cross-validation to distinguish borehole-scale variability from spatially predictable structure. Independently, a large regional strong-motion database is decomposed into event, path, and site contributions to quantify the dependence of PGA and spectral amplification on Vs30 and to examine

how this dependence varies with earthquake magnitude and reference-rock input-motion intensity. The resulting relationships are transferred to the borehole-constrained digital soil field with explicit propagation of subsurface, spatial-prediction, and amplification-model uncertainty.

The framework uses the mapped Vs30 field as a spatial substrate whose seismic expression is conditioned by spectral period, earthquake magnitude, and input-motion intensity. The ensemble SPT–Vs transformation, uncertainty propagation, and observation-based magnitude–period decomposition together enable multiple response states to be generated from the same subsurface field. This formulation extends Vs30-based site characterization toward response-oriented digital soil mapping.

2. Data and methodology

The analytical framework combines two independent sources of information: a borehole-based SPT database used to construct a digital representation of shallow soil stiffness, and a regional strong-motion database used to derive observational relationships between site condition and seismic amplification. Because the two datasets are not spatially coincident, they were not merged on a point-to-point basis. The SPT data were first transformed into a spatial Vs30 proxy field, whereas the strong-motion data were independently used to establish empirical Vs30-dependent amplification relationships. These relationships were subsequently transferred to the digital soil field to obtain magnitude- and period-dependent amplification layers. The overall data configuration is shown in Figure 1, and the principal characteristics of the datasets are summarized in Table 1. The borehole study area occupies a compact urban coastal-alluvial sector on the northern side of İzmir Bay, centered on the Karşıyaka urban area. The 50 borehole locations extend from 38.4509° to 38.4786° N and from 27.0679° to 27.1285° E, and their convex hull covers approximately 7.6 km². The borehole archive contains 678 depth-resolved SPT observations, together with fines content, plasticity index, groundwater depth, and borehole coordinates. SPT resistance and borehole coordinates were used directly in the velocity transformation and spatial modeling, whereas the remaining variables were retained for data auditing and contextual interpretation.

The regional strong-motion flatfile spans the period from January 30, 1996, to October 28, 2025. After matching the records with the available station metadata, the analysis database comprised 15,483 records from 1366 earthquakes recorded at 34 stations. The station network extends approximately from 37.94° to 39.11° N and from 26.37° to 27.96° E, with station Vs30 values ranging from 131 to 875 m/s. PGA was used as reported in the source flatfile, whereas the horizontal spectral ordinates at T = 0.1, 0.5, 1.0, 2.0, and 3.0 s were represented by the geometric mean of the east–west and north–south components. Records were retained when station and event identifiers, magnitude, epicentral distance, focal depth, and a positive value of the relevant intensity measure were available. The records were obtained from AFAD–TADAS/Turkish National Strong Motion Network [16].

2.1. SPT database and derivation of borehole-scale Vs30

The subsurface database consists of 50 boreholes distributed within the urban alluvial study area. The available information includes depth-resolved SPT resistance together with fines content, plasticity information, groundwater data, and borehole coordinates. Quality control was performed

prior to the velocity transformation. Records with missing depth or SPT resistance were excluded from the dynamic-property calculation, physically inadmissible fines-content values were treated as missing values, and the original depth sequence of each borehole was retained.

Four established all-soil SPT–Vs relationships were used as an ensemble rather than adopting a single deterministic transformation (Table 2). The selected formulations represent widely used empirical relationships reported in the SPT–Vs literature [8,9,17,18] and subsequently evaluated comparatively by Dikmen [10].

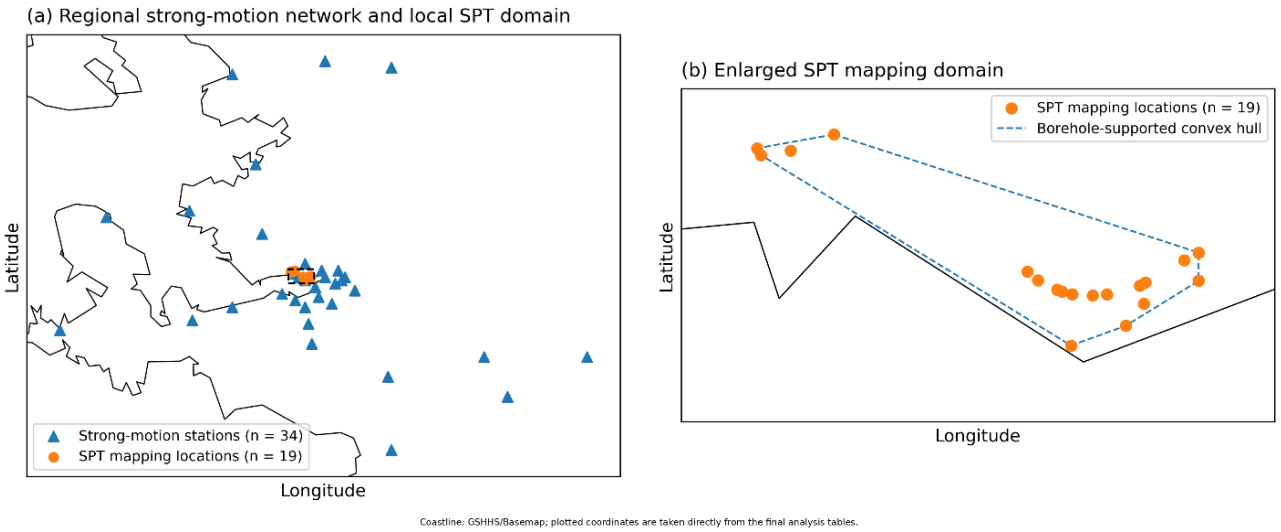

Figure 1. Spatial configuration of the datasets used in the study: (a) regional distribution of the 34 strong-motion stations used to derive the empirical Vs30–amplification relationships, with the compact borehole study domain indicated by the dashed box; (b) enlarged view of the 19 unique SPT mapping locations and their borehole-supported convex hull. The strong-motion and borehole datasets were analyzed independently and integrated only at the response-transfer stage. Coastline data are shown for geographic context.

Table 1. Principal characteristics of the datasets used in the analysis.

Component	Dataset characteristics
Original SPT boreholes	50
SPT observations	678
Boreholes reaching at least 20 m	25
Boreholes reaching at least 30 m	10
Unique locations retained for final digital mapping	19
Matched strong-motion records	15,483
Earthquakes represented in strong-motion database	1366
Strong-motion stations	34
Intensity measures	PGA, Sa(0.1), Sa(0.5), Sa(1.0), Sa(2.0), Sa(3.0)
Magnitude groups	Mw = 3.0–3.9, 4.0–4.9, 5.0–5.9, ≥6.0

Table 2. Empirical SPT–Vs relationships used to construct the velocity ensemble.

Relationship	Adopted equation, Vs in m/s
Imai and Yoshimura	$Vs = 76\ N^{0.33}$
Ohta and Goto	$Vs = 85.35\ N^{0.348}$
Imai and Tonouchi	$Vs = 97\ N^{0.314}$
Hasancebi and Ulusay	$Vs = 90\ N^{0.309}$

As an independent regional geophysical consistency check, the shallow-velocity levels obtained from the SPT-based transformation were compared with an available SPAC-derived shear-wave velocity profile representative of the İzmir Bay alluvial setting (S. Altun, unpublished technical assessment). The SPAC interpretation indicates Vs values of approximately 200–250 m/s within the upper 30 m. This independent geophysical range was used to evaluate the regional plausibility of the SPT-derived digital Vs30 field and was not included in model calibration.

Each borehole profile was discretized at 0.25 m intervals, and the nearest measured SPT resistance was assigned to each interval rather than linearly interpolating between tests. This treatment preserves the piecewise stratigraphic character of the borehole information and avoids introducing artificial intermediate penetration resistance values.

The four SPT–Vs equations were then applied independently, and Vs30 was calculated from the standard travel-time average:

$$Vs30 = 30 / \Sigma(hi / Vs,i)$$

For each borehole, the median of the four Vs30 estimates was adopted as the central proxy, while the 16th and 84th percentiles were retained as a measure of between-correlation model-form spread. Boreholes shallower than 30 m were handled through a masked-validation procedure. The 10 profiles extending to at least 30 m were artificially truncated at 20 m and reconstructed using alternative 20–30 m completion strategies. The reconstructed Vs30 values were compared directly with those obtained from the full profiles, providing a data-based basis for selecting the lower-profile completion method subsequently applied to boreholes extending between 20 and 30 m. Boreholes shallower than 20 m were excluded from the final Vs30 estimation and mapping, because the completion strategy was validated only for the 20–30 m interval. The sensitivity of the final digital Vs30 and amplification fields to this choice was subsequently evaluated by repeating the complete transfer procedure using the alternative P25, P50, and P75 regional depth-prior completion strategies.

2.2. Digital mapping of the SPT-derived Vs30 field

Only boreholes providing sufficient depth coverage for the validated Vs30 calculation were retained for spatial analysis. Where multiple boreholes shared the same coordinates, they were treated as repeated observations of one spatial location rather than as independent spatial samples. The median Vs30 proxy was therefore calculated for each coordinate, resulting in 19 unique locations for the final digital mapping analysis.

Three spatial prediction methods were compared: inverse-distance weighting (IDW), ordinary kriging, and Gaussian process regression. IDW was evaluated over several distance-decay exponents; ordinary kriging used a spherical variogram representation; and Gaussian process regression used a

Matérn covariance structure with an explicit noise component. Spatial predictive performance was assessed using leave-one-location-out cross-validation. All boreholes associated with the test coordinate were excluded simultaneously, preventing colocated observations from appearing in both calibration and validation subsets. Model selection was based primarily on cross-validated RMSE, with MAE, bias, Pearson correlation, and predictive R^2 used as complementary diagnostics.

The method yielding the lowest cross-validated RMSE was retained for construction of the continuous Vs30 proxy field. Predictions were restricted to the convex hull defined by the unique borehole locations so that the digital soil representation did not extrapolate beyond the spatial support of the data. The spatial prediction uncertainty was retained at each grid cell for subsequent propagation into the seismic amplification calculations. Relative spatial prediction uncertainty was additionally calculated as the local prediction standard deviation divided by the predicted Vs30 and expressed as a percentage.

The selected interpolator provides a borehole-constrained spatial representation of the shallow stiffness field. Location-based cross-validation and prediction uncertainty are retained throughout the subsequent response-transfer analysis to characterize the spatial resolution supported by the available observations.

2.3. Strong-motion decomposition and empirical amplification model

The seismic-response component was derived independently from the regional strong-motion database. After matching recordings with station metadata, the database comprised 15,483 records from 1366 earthquakes recorded at 34 stations with available Vs30 information. PGA and geometric-mean horizontal spectral accelerations at T = 0.1, 0.5, 1.0, 2.0, and 3.0 s were considered so that site response could be evaluated across the response spectrum rather than through a single PGA-based amplification factor. The distribution of records, earthquakes, and contributing stations among the four magnitude groups used in the stratified analyses is summarized in Table 3.

Table 3. Distribution of strong-motion records, earthquakes, and contributing stations among the magnitude groups used in the magnitude-stratified analyses.

Magnitude group	Records	Earthquakes	Stations
Mw = 3.0–3.9	8585	829	34
Mw = 4.0–4.9	5498	427	34
Mw = 5.0–5.9	1123	93	34
Mw ≥ 6.0	277	17	34

The number of records and earthquakes decreases with increasing magnitude, with the Mw ≥ 6.0 group represented by 277 records from 17 earthquakes. All four magnitude groups include observations from the same 34 stations.

The empirical model was formulated in logarithmic space and referenced to $V_{s30} = 760$ m/s. For earthquake e, station s, and an intensity measure at period T, the continuous model was written as

$$\ln Y_{es,T} = \alpha_{e,T} + \beta_{R1,T}\ln R_{\mathrm{eff},es} + \beta_{R2,T}\left(\frac{R_{\mathrm{epi},es}}{100}\right) + \beta_{D,T}\left(\frac{D_e}{20}\right) + \beta_{V,T}X_s + \beta_{M1,T}X_s M_{c,e} + \beta_{M2,T}X_s M_{c,e}^2 + \varepsilon_{es,T}.$$

where

$$X_s = \ln\left(\frac{V_{s30,s}}{760}\right), \qquad M_{c,e} = M_e - 4.5,$$

and

$$R_{\mathrm{eff},es} = \sqrt{R_{\mathrm{epi},es}^2 + 10^2}.$$

Here, $Y_{es,T}$ denotes PGA or the geometric-mean horizontal spectral acceleration, $\alpha_{e,T}$ is an unrestricted event-specific intercept, R_{epi} is epicentral distance in kilometres, and D_e is focal depth in kilometres. The within-event transformation removes $\alpha_{e,T}$ before estimation. Event-level main effects, including the magnitude main effect, are consequently absorbed by the event intercept, while the magnitude-site interaction remains estimable from within-event station-to-station variation.

The corresponding amplification relative to the $V_{s30} = 760$ m/s reference condition was expressed as

$$AF(T, M, V_{s30}) = \exp\left\{\left[\beta_{V,T} + \beta_{M1,T}M_c + \beta_{M2,T}M_c^2\right]\ln\left(\frac{V_{s30}}{760}\right)\right\}.$$

The site coefficient was allowed to vary with magnitude through the linear and quadratic magnitude–Vs30 interaction terms in Equation (1). Independent regressions were also fitted for the magnitude groups Mw = 3.0–3.9, 4.0–4.9, 5.0–5.9, and Mw ≥ 6.0. These magnitude-stratified models provided a direct check on the continuous interaction formulation and were subsequently used for scenario mapping without requiring interpolation between magnitude groups.

Uncertainty in the magnitude-stratified site slopes was evaluated using an event-balanced cluster bootstrap. Earthquakes were resampled with replacement while all station records belonging to a selected event were retained together. A second robustness check was obtained from repeatable station-level amplification terms, which were independently regressed against station Vs30. Because Vs30 is a station-level attribute, and multiple records were available from individual stations, dependence was additionally evaluated using two-way event- and station-clustered covariance estimates. Leave-one-station-out refits were also performed to assess the sensitivity of the inferred site coefficients to individual stations. Agreement among the within-event model, magnitude-group regressions, bootstrap distributions, station-level relationships, clustered inference, and leave-one-station-out results was used to assess the stability of the inferred site dependence.

Because earthquake magnitude and input-motion amplitude are correlated, an additional sensitivity analysis was performed to distinguish magnitude-associated modulation from amplitude-dependent site response. Reference-rock motion was reconstructed independently for each intensity measure from the static-site version of Equation (1), in which the path terms and the linear V_{s30} term

were retained. The event intercept was recovered as the event-specific mean residual after subtraction of the fitted path and site contributions. Setting $X_s = 0$, corresponding to $V_{s30} = 760$ m/s, yielded

$$\ln I_{\mathrm{rock},es,T} = \hat{\alpha}_{e,T} + \hat{\beta}_{R1,T} \ln R_{\mathrm{eff},es} + \hat{\beta}_{R2,T} \left(\frac{R_{\mathrm{epi},es}}{100}\right) + \hat{\beta}_{D,T} \left(\frac{D_e}{20}\right).$$

The resulting reference-rock intensity is therefore a record-specific empirical model quantity evaluated for the same event and path conditions as the observation; it is not a directly recorded rock-site motion. For the joint magnitude-intensity analysis, reference-rock intensity was centered as:

$$P_{es,T} = \ln I_{\mathrm{rock},es,T} - \mathrm{median}\left[\ln I_{\mathrm{rock},T}\right].$$

The full joint formulation augmented the path and static site terms with linear and quadratic magnitude- and intensity-dependent interactions:

$$\begin{aligned} \ln Y_{es,T} = {} & \alpha_{e,T} + \text{path terms} + \gamma_{V,T} X_s \\ & + \gamma_{M1,T} X_s M_{c,e} + \gamma_{M2,T} X_s M_{c,e}^2 \\ & + \gamma_{I1,T} X_s P_{es,T} + \gamma_{I2,T} X_s P_{es,T}^2 + \varepsilon_{es,T}. \end{aligned}$$

Four nested formulations were compared: the static V_{s30} model (M0); the magnitude-interaction model containing the two $X_s M_c$ terms (MM); the intensity-interaction model containing the two $X_s P_T$ terms (MI); and the full model containing both interaction families (MF). The primary analysis used the corresponding reference-rock spectral ordinate for each response measure, while reference-rock PGA was additionally evaluated as a common broadband intensity proxy. Model fit, residual error, information criteria, and joint significance tests were used to compare the four formulations. Event-balanced bootstrap resampling was used to assess the stability of the magnitude- and intensity-dependent interactions.

Because long-period site response may also reflect deeper site structure, an additional sensitivity analysis was performed using station fundamental frequency f_0 as an available proxy for site-period and deeper-structure effects. The relationship between $\ln(V_{s30}/760)$ and $\ln(f_0)$ was first examined to assess redundancy between the two site descriptors. The long-period magnitude–V_{s30} interaction was then re-estimated using two collinearity-aware formulations: f_0 included as a main-effect control and the residual component of f_0 after regression against V_{s30}. These formulations were used to evaluate whether the magnitude-associated interaction at 2.0–3.0 s persisted after accounting for the independent information contained in the available fundamental-frequency proxy.

2.4. Transfer to the digital soil field and uncertainty propagation

The final integration was performed only after the SPT-based digital field and the observational strong-motion relationships had been established independently. At each grid cell, the mapped Vs30 proxy was introduced into the empirical amplification function to produce a family of magnitude- and period-dependent amplification layers. The procedure was applied to 6 intensity measures and 4 magnitude groups, producing 24 scenario-dependent fields from a single digital soil representation.

Uncertainty was propagated in logarithmic V_{s30} space. At grid cell g, the central spatial prediction was denoted by $\hat{V}_{s30,g}$. The between-correlation component was represented by

$$\sigma_{\mathrm{SPT},g} = \frac{\ln V_{s30,g}^{(84)} - \ln V_{s30,g}^{(16)}}{2},$$

where the borehole-scale 16th–84th percentile spread across the four SPT-V_s relationships was interpolated to the grid. This quantity was treated as an operational representation of SPT-V_s model-form variability rather than as a formal probabilistic confidence interval. The additive spatial prediction standard deviation, s_g, was converted to logarithmic form as:

$$\sigma_{\mathrm{spatial},g} = \sqrt{\ln\left[1 + \left(\frac{s_g}{\hat{V}_{s30,g}}\right)^2\right]}.$$

For Monte Carlo realization k, a positive V_{s30} value was generated as

$$\ln V_{s30,g}^{(k)} = \ln \hat{V}_{s30,g} + \eta_{\mathrm{SPT},g}^{(k)} + \eta_{\mathrm{spatial},g}^{(k)},$$

with

$$\eta_{\mathrm{SPT},g}^{(k)} \sim N\left(0, \sigma_{\mathrm{SPT},g}^2\right), \qquad \eta_{\mathrm{spatial},g}^{(k)} \sim N\left(0, \sigma_{\mathrm{spatial},g}^2\right).$$

Amplification-slope uncertainty was represented by a normal approximation to the event-bootstrap distribution. For each intensity-measure and magnitude-group combination,

$$\beta_T^{(k)} \sim N\left(\tilde{\beta}_{T,\mathrm{boot}}, \sigma_{\beta,T}^2\right), \qquad \sigma_{\beta,T} = \frac{\beta_{T,\mathrm{boot}}^{97.5} - \beta_{T,\mathrm{boot}}^{2.5}}{3.92}.$$

One amplification-slope realization was applied across all grid cells within a given scenario and Monte Carlo iteration, preserving the scenario-wide coherence of model uncertainty. Cell-specific SPT-V_s and spatial perturbations were sampled independently, and the three uncertainty sources were assumed to be mutually independent. To examine the influence of dependence among the propagated uncertainty components, additional sensitivity cases were evaluated using moderate positive correlation (ρ = 0.5), perfect positive correlation between the SPT–V_s and spatial-prediction components, and an all-perfect-positive upper-bound case.

Spatial cross-covariance among prediction errors was not simulated. The amplification realization was then calculated as

$$AF_{g,T}^{(k)} = \exp\left[\beta_T^{(k)} \ln\left(\frac{V_{s30,g}^{(k)}}{760}\right)\right].$$

A total of 5000 realizations was generated for every grid cell, intensity measure, and magnitude scenario. The 16th, 50th, and 84th percentiles of the resulting amplification distribution were retained. To decompose the propagated uncertainty, the simulation was repeated with only the SPT-V_s, spatial-prediction, or amplification-model component active, followed by the fully combined case. Relative uncertainty was calculated as

$$U_{68} = 100\,\frac{AF_{84} - AF_{16}}{2AF_{50}}.$$

To summarize the magnitude-associated contrast independently of the absolute amplification level, a magnitude-modulation ratio was calculated as the amplification predicted for Mw ≥ 6.0 divided by that for Mw = 3.0–3.9 at the same grid cell and spectral period. This transfer preserves the separation between subsurface characterization and observational seismic response while allowing their respective uncertainties to be propagated into the final amplification fields.

The resulting layers are therefore treated as scenario-dependent, borehole-constrained empirical amplification fields rather than as deterministic amplification zoning. This distinction provides the basis for the Results section, where the spatial predictability of the Vs30 field, the strength of the observed Vs30–amplification relationships, and the period-dependent roles of magnitude-associated and input-intensity-dependent modulation are evaluated quantitatively.

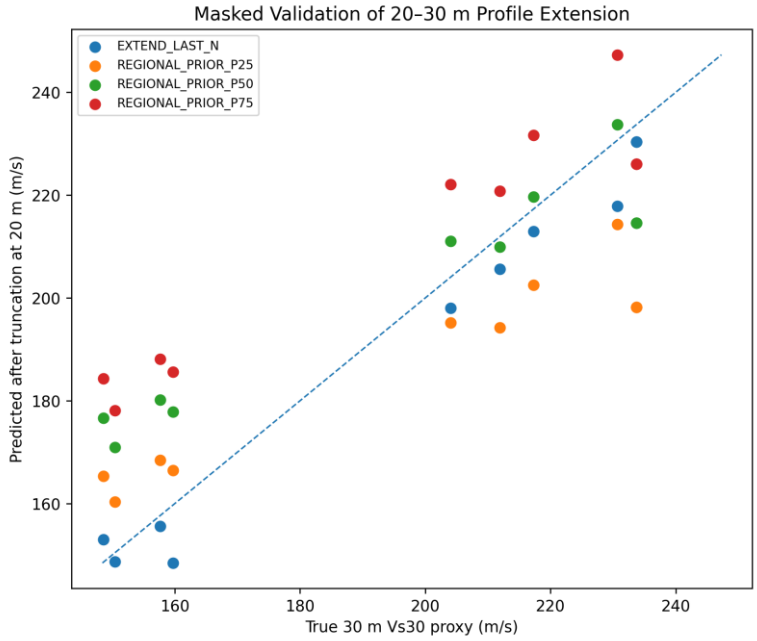

Figure 2. Masked validation of the lower-profile completion procedure. Boreholes extending beyond 30 m were artificially truncated at 20 m, reconstructed using alternative 20–30 m completion strategies, and compared with the Vs30 proxies calculated from the complete profiles. The dashed line represents perfect agreement.

3. Results

3.1. Validation and spatial structure of the SPT-derived Vs30 field

The first stage of the analysis evaluated whether boreholes terminating between 20 and 30 m could be incorporated into the digital Vs30 model without introducing substantial bias. Masked validation was performed using the boreholes that actually extended to at least 30 m. When these

profiles were artificially truncated at 20 m, continuation of the deepest observed SPT resistance produced the closest reconstruction of the complete-profile Vs30 values. The resulting RMSE was 6.60 m/s, and the predictive R2 was 0.963, substantially outperforming the regional depth-prior alternatives. The comparison in Figure 2 shows that the reconstructed values remain closely distributed around the 1:1 line, indicating that the lower 10 m contributes relatively limited additional uncertainty to Vs30 within the investigated alluvial profiles.

To assess whether the final response products were sensitive to the assumed 20–30 m profile completion, the full analysis was repeated using three alternative regional depth-prior strategies (P25, P50, and P75) in place of the selected deepest-observed-SPT continuation. At the borehole scale, the largest median absolute change in V_{s30} was 3.10%, although larger differences occurred for a limited number of profiles, with a 95th-percentile absolute change of 13.57%. After spatial interpolation, the corresponding median grid-scale differences reached at most 7.55%, with a 95th-percentile difference of 8.82%. For the $Mw \geq 6.0$ amplification scenarios, the largest median absolute change among all intensity measures was 7.06%, and the corresponding 95th-percentile change was 8.36%. These differences remain smaller than the propagated uncertainty of the final amplification fields, indicating that the principal response patterns are not strongly dependent on the selected lower-profile completion strategy.

The validated profile-completion procedure enabled 25 sufficiently deep boreholes to be retained for Vs30 estimation. After colocated boreholes were aggregated, 19 unique locations were used for spatial modeling. The resulting borehole-scale Vs30 proxies indicate appreciable borehole-scale variability within the alluvial field, but the strict spatial validation provides a different perspective on the predictability of this variation. Ordinary kriging yielded the lowest leave-one-location-out error, with an RMSE of 28.59 m/s and an MAE of 23.87 m/s; however, the corresponding predictive R^2 was only 0.117 (Table 4). IDW and Gaussian-process predictions produced similar error levels and did not materially improve the location-independent prediction.

Table 4. Validation performance of the SPT-derived digital soil model.

Validation component	Best-performing method	RMSE (m/s)	MAE (m/s)	Predictive R^2
20–30 m profile completion	Deepest observed SPT-N extension	6.60	5.56	0.963
Strict unique-location spatial mapping	Ordinary kriging	28.59	23.87	0.117

To examine whether the limited spatial predictability could be improved using the available auxiliary information, an additional strict leave-one-location-out sensitivity analysis was performed using groundwater depth, fines content, plasticity index, and spatial coordinates. The best-performing auxiliary model, an Extra Trees regressor, reduced the RMSE from 28.59 to 27.13 m/s and increased the predictive R^2 from 0.117 to 0.204. This corresponds to a 5.1% reduction in RMSE and therefore represents only a modest improvement in location-independent prediction. The individual auxiliary variables also showed weak-to-moderate correlations with the borehole-scale V_{s30} proxy. Within the set of auxiliary variables evaluated here, the modest improvement indicates that sparse spatial support remains the primary constraint on location-independent prediction.

This spatial behavior is visible in Figure 3a, where the mapped field exhibits broad variations in inferred shallow stiffness. Figure 3b shows the corresponding absolute spatial prediction uncertainty, while Figure 3c expresses the same uncertainty relative to the predicted V_{s30}. Relative uncertainty ranges approximately from 12.5% to 14.4% across the borehole-supported domain, providing a direct measure of the spatial confidence associated with the interpolated field.

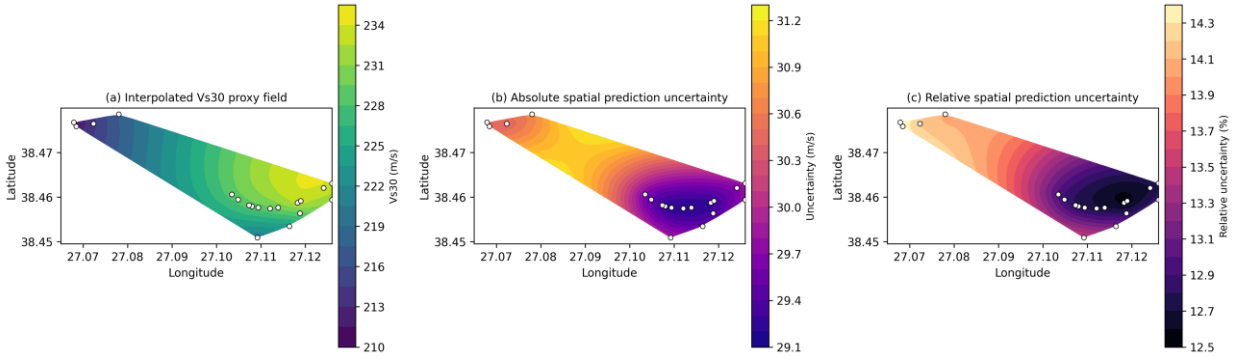

Figure 3. Digital representation of the SPT-derived V_{s30} field: (a) interpolated V_{s30} proxy field based on the unique borehole locations, (b) corresponding absolute spatial prediction uncertainty, and (c) relative spatial prediction uncertainty expressed as a percentage of the predicted Vs30. Predictions are restricted to the convex hull of the borehole network.

The independent SPAC comparison further constrained the absolute velocity level represented by the digital soil field. As summarized in Table 5, the mapped Vs30 interval lies entirely within the upper-30-m SPAC velocity range reported for the İzmir Bay alluvial setting (S. Altun, unpublished technical assessment), while the representative value of the digital field closely coincides with the center of this independent geophysical benchmark. The comparison therefore supports the regional consistency of the shallow-stiffness level represented by the SPT-derived field.

Table 5. Regional geophysical consistency of the SPT-derived digital Vs30 field.

Comparison	SPAC benchmark	SPT-derived result	Difference/overlap
Upper-30-m velocity range	200–250 m/s	211–234 m/s	Complete overlap
Central-value comparison	225 m/s	223 m/s	2 m/s (0.9%)
Coverage of mapped Vs30 range	200–250 m/s	211–234 m/s	100% within SPAC range

These results support the use of the digital field as a borehole-constrained representation of broad stiffness gradients with explicitly retained spatial prediction uncertainty.

3.2. Observed Vs30–amplification relationships

The strong-motion analysis produced a consistent inverse relationship between Vs30 and empirical amplification for all investigated intensity measures. The site coefficient βVs30 was negative

for PGA and for all spectral accelerations from 0.1 to 3.0 s, indicating systematically larger amplification at lower Vs30. This dependence was statistically significant in all cases (Table 6).

The strength of the site dependence increased from PGA toward intermediate and longer spectral periods. The continuous within-event model yielded βVs30 = −0.417 for PGA, while the corresponding coefficients reached −0.738, −0.841, and −0.824 for Sa(1.0s), Sa(2.0s), and Sa(3.0s), respectively. The within-event models explained approximately 33%–50% of the station-to-station variation remaining after removal of event effects.

A separate station-level analysis provided an independent check on the same relationship. Repeatable station terms were strongly correlated with Vs30, particularly from 0.5 to 3.0 s. Station-term R^2 values were 0.704 at 0.5 s, 0.753 at 1.0 s, 0.724 at 2.0 s, and 0.687 at 3.0 s. The corresponding Pearson correlations ranged from approximately −0.83 to −0.87, confirming that the observed spectral site-response pattern was not an artifact of a single regression formulation.

Table 6. Strong-motion Vs30 dependence and dependence-aware magnitude–site interaction statistics.

IM	βVs30	p for Vs30 effect, two-way clustered	p for magnitude–site interaction, two-way clustered	Within-event R^2	Station-term R^2
PGA	−0.417	1.45×10^{-8}	3.15×10^{-5}	0.334	0.327
Sa(0.1 s)	−0.263	0.00639	2.45×10^{-5}	0.330	0.193
Sa(0.5 s)	−0.602	1.65×10^{-25}	0.211	0.403	0.704
Sa(1.0 s)	−0.738	9.07×10^{-30}	0.151	0.482	0.753
Sa(2.0 s)	−0.841	9.18×10^{-23}	0.00321	0.495	0.724
Sa(3.0 s)	−0.824	2.77×10^{-19}	6.91×10^{-7}	0.465	0.687

Note: Reported significance levels for the Vs30 main effect and magnitude–site interaction are based on two-way covariance clustering by earthquake and station. Station-term R^2 values are obtained independently from regressions of repeatable station effects against station Vs30.

Because Vs30 is a station-level predictor represented repeatedly across earthquake records, the stability of these relationships was further evaluated using dependence-aware inference. After simultaneous clustering by earthquake and station, the Vs30 effect remained statistically significant for all investigated intensity measures. The magnitude–site interaction also remained significant for PGA, Sa(0.1s), Sa(2.0s), and Sa(3.0s), whereas it was not significant at Sa(0.5s) and Sa(1.0s). Leave-one-station-out refits produced consistently negative Vs30 coefficients for every intensity measure, with only limited variation around the full-data estimates. The inferred site dependence was therefore robust to the influence of individual stations and to dependence induced by repeated observations.

The magnitude-group relationships shown in Figure 4 further demonstrate that the Vs30–amplification relation does not evolve uniformly across the response spectrum. For PGA, the magnitude-group curves progressively separate as earthquake magnitude increases, indicating stronger relative amplification at soft sites during larger events. A similarly clear separation is observed at long periods, especially at 2.0 and 3.0 s. In contrast, the curves at 0.5–1.0 s remain much closer together, despite the persistence of a strong overall Vs30 effect. The graphical pattern therefore suggests that the role of earthquake magnitude is itself period-dependent.

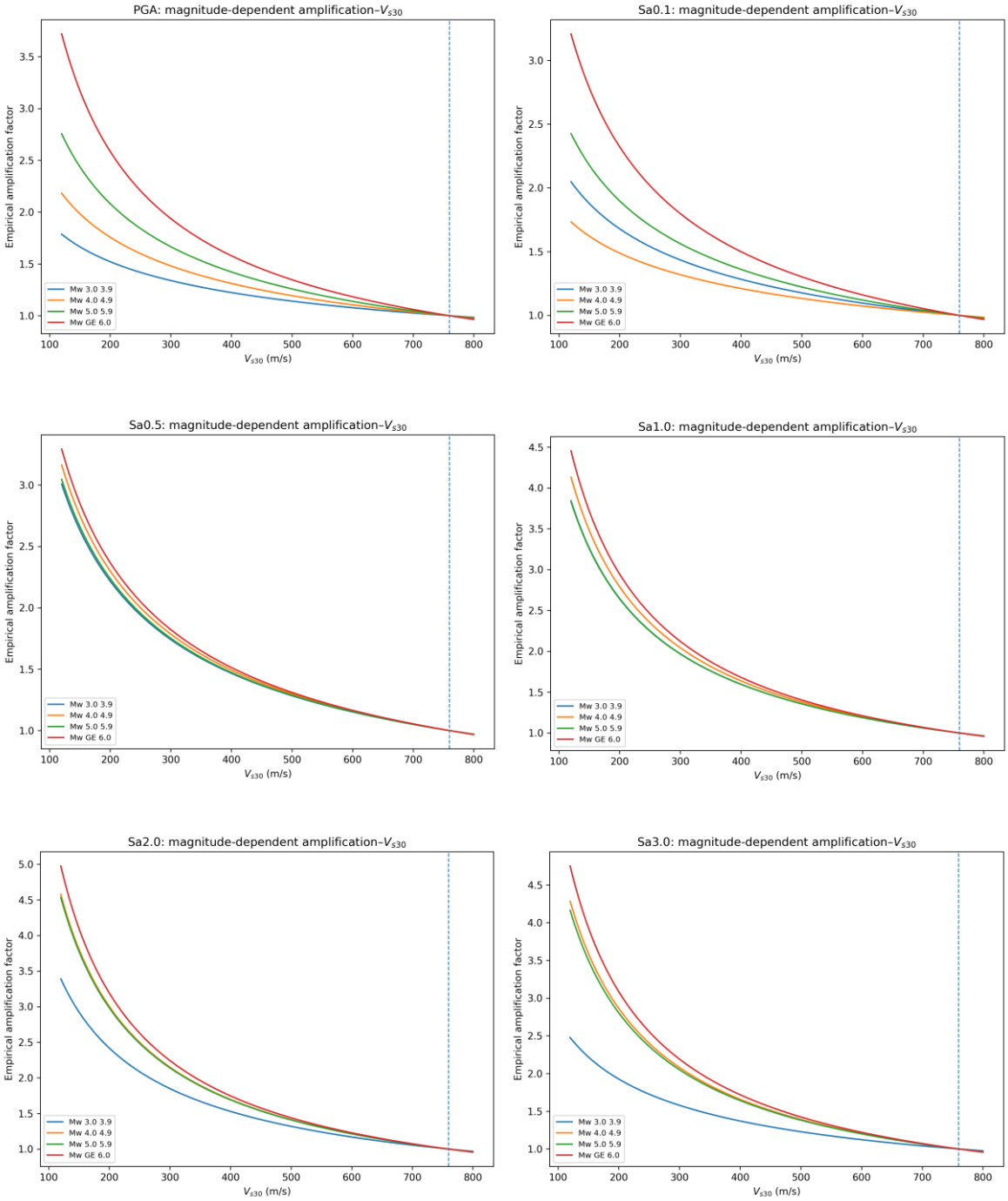

Figure 4. Empirical relationship between Vs30 and seismic amplification for different earthquake-magnitude groups: (a) PGA, (b) Sa(0.5s), (c) Sa(1.0s), (d) Sa(2.0s), and (e) Sa (3.0s). Amplification is referenced to Vs30 = 760 m/s.

Taken together, these results establish two robust features of the strong-motion dataset: first, lower Vs30 is consistently associated with stronger amplification across all investigated intensity measures, and this relationship remains stable under event- and station-aware robustness tests; second, the extent to which the Vs30–amplification relationship varies with earthquake magnitude is not uniform across the response spectrum. This second feature motivates the next section, where

the period dependence of magnitude-associated modulation is examined more explicitly and tested against input-motion intensity.

3.3. Period dependence of magnitude and input-motion modulation

The magnitude-stratified analysis showed that the contrast between soft- and reference-site amplification varies substantially across the response spectrum. When expressed as the ratio between the amplification associated with Mw ≥ 6.0 and that associated with Mw = 3.0–3.9, the magnitude-modulation ratio is approximately 1.63 for PGA and 1.35 at 0.1 s, decreases to 1.06 at 0.5 s and 1.10 at 1.0 s, and subsequently increases to 1.29 at 2.0 s and 1.54 at 3.0 s. As shown in Figure 5, the resulting response therefore exhibits a distinctly non-uniform spectral pattern rather than a uniform magnitude-dependent scaling of site amplification.

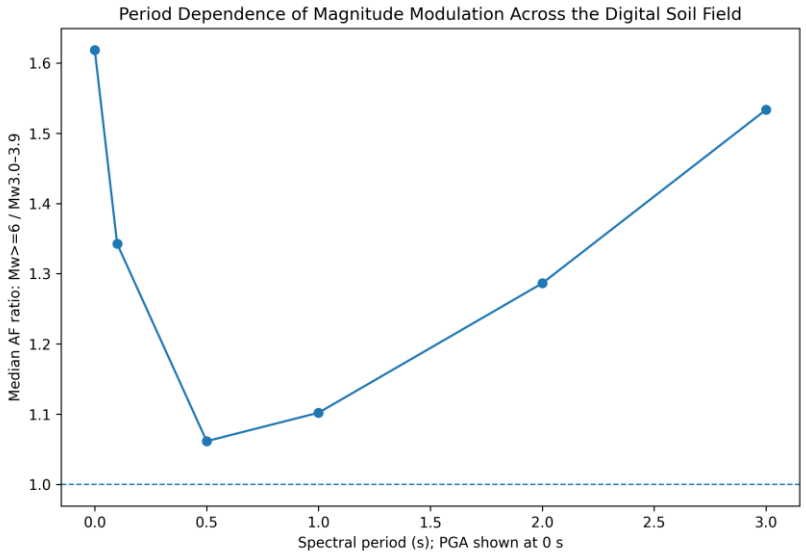

Figure 5. Period dependence of earthquake-magnitude modulation, expressed as the ratio between empirical amplification predicted for Mw ≥ 6.0 and Mw = 3.0–3.9 at the representative Vs30 of the digital soil field. PGA is plotted at T = 0 s solely for visualization.

The corresponding amplification values are summarized in Table 7. At the representative Vs30 of the digital soil field, PGA amplification increases from 1.47 in the smallest magnitude group to 2.39 for Mw ≥ 6.0, while the corresponding values at 3.0 s increase from 1.83 to 2.82. At 0.1 s, the magnitude-modulation ratio remains appreciable at 1.35. By contrast, amplification at 0.5 s changes only from 2.08 to 2.21, with a similarly limited contrast at 1.0 s. The magnitude-group separation is therefore strongest for PGA and longer-period response, reaches an intermediate level at 0.1 s, and is weakest around 0.5–1.0 s.

The spectral modulation pattern was preserved when station composition was held constant across magnitude groups. Restricting the Mw = 3.0–3.9 and Mw ≥ 6.0 comparison to the common stations reproduced the full-data amplification ratios, confirming the stability of the observed spectral dependence across the shared station population.

A regional-to-local transfer sensitivity analysis was subsequently performed by re-estimating the magnitude-dependent amplification relationships for geographically restricted and site-condition-restricted station subsets. Restricting the analysis to stations within 25, 50, and 75 km of the borehole domain preserved the full-network spectral modulation pattern closely, with pattern correlations of r = 0.993, 0.991, and 0.999, respectively. The corresponding median absolute differences in the modulation ratio were 2.09%, 2.99%, and 0.62%. When the analysis was restricted to a 17-station soft-site subset broadly comparable with the local Vs30 range, the spectral pattern also remained strongly correlated with the full-network result (r = 0.970), although the absolute modulation ratios differed more substantially, with a median absolute difference of 27.27%. These results indicate that the period-dependent organization of the response is relatively stable under regional-to-local restriction, whereas the absolute amplification level remains more sensitive to station population and site-condition selection.

Table 7. Amplification factors and magnitude-modulation ratios evaluated at the representative Vs30 of the digital soil field.

IM	AF, Mw = 3.0–3.9	AF, Mw ≥ 6.0	AF ≥ 6 / AF 3.0–3.9
PGA	1.47	2.39	1.63
Sa(0.1s)	1.61	2.17	1.35
Sa(0.5s)	2.08	2.21	1.06
Sa(1.0s)	2.45	2.7	1.1
Sa(2.0s)	2.25	2.9	1.29
Sa(3.0s)	1.83	2.82	1.54

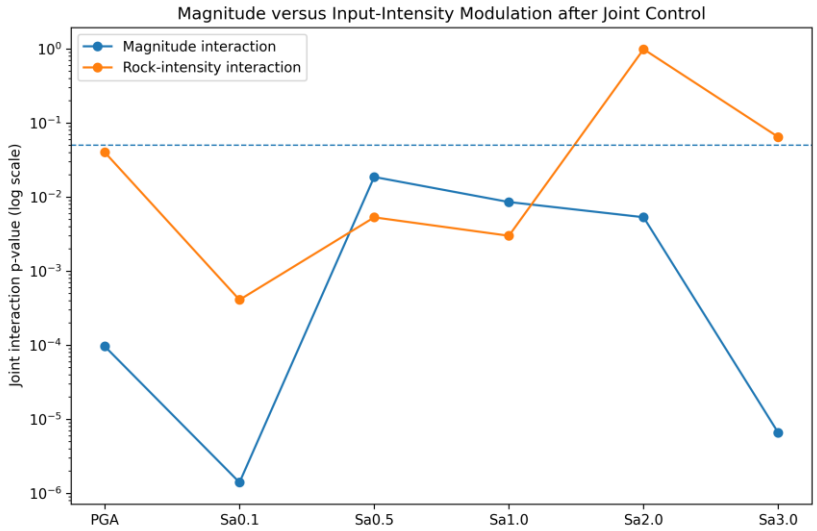

Figure 6. Joint significance of magnitude–Vs30 and reference-rock-intensity–Vs30 interactions across PGA and spectral periods. The dashed horizontal line denotes the p = 0.05 significance level.

Because earthquake magnitude and input-motion amplitude are correlated, the magnitude-associated pattern was further examined after explicitly introducing reference-rock intensity into the site-response model. The correlation between magnitude and the corresponding reference-rock motion

was moderate to strong and varied across the response spectrum. Nevertheless, in the full joint model, the magnitude–Vs30 interaction remained statistically significant after simultaneous control for the corresponding reference-rock intensity for PGA, Sa(0.1s), Sa(2.0s), and Sa(3.0s), with joint p-values of 9.62×10^{-5}, 8.39×10^{-7}, 0.00549, and 5.59×10^{-6}, respectively.

The intermediate-period response showed a different pattern. At 0.5 and 1.0 s, both magnitude and the corresponding reference-rock spectral intensity contributed significantly to modulation of the Vs30 site term. At 0.5 s, the joint-model p-values were 0.0210 for the magnitude interaction and 0.00591 for the spectral-intensity interaction; at 1.0 s, they were 0.00891 and 0.00345, respectively. In contrast, the same-period intensity interaction was negligible at 2.0 s ($p = 0.977$), despite persistence of the magnitude interaction ($p = 0.00549$), and was not statistically significant at 3.0 s ($p = 0.0730$). These results indicate that corresponding spectral input-motion intensity contributes most clearly to modulation in the intermediate-period range, whereas magnitude-associated modulation remains more persistent toward longer periods.

Figure 6 summarizes the contrasting spectral roles of the magnitude- and reference-rock-intensity interactions.

Event-balanced bootstrap resampling supported the same period-dependent pattern. Magnitude-associated effects received the strongest support for PGA and longer-period response, whereas reference-rock intensity showed its strongest influence at intermediate periods. The joint-model significance levels and bootstrap support are summarized in Table 8.

Table 8. Joint magnitude- and reference-rock-intensity interaction tests.

IM	p, magnitude interaction	p, same-period rock–intensity interaction	Bootstrap support: magnitude	Bootstrap support: intensity	Interpretation
PGA	9.62×10^{-5}	0.04	1.00	0.42	Predominantly magnitude-associated
Sa(0.1s)	8.39×10^{-7}	3.5×10^{-4}	1.00	0.99	Mixed magnitude–intensity
Sa(0.5s)	0.021	0.00591	0.58	0.96	Predominantly spectral-intensity conditioned
Sa(1.0s)	0.00891	0.00345	0.97	1.00	Mixed magnitude–intensity
Sa(2.0s)	0.00549	0.977	0.86	0.00	Predominantly magnitude-associated
Sa(3.0s)	5.59×10^{-6}	0.073	1.00	0.3	Predominantly magnitude-associated

The bootstrap result can be inspected in more detail in Figure 7, which shows the frequency-dependent support for the two interaction terms across repeated event-balanced resamples.

Because the long-period response may also reflect deeper site structure, an additional robustness analysis was performed using station fundamental frequency f_0 as an available proxy for site-period and deeper-structure effects. At the station level, $\ln(V_{s30}/760)$ and $\ln(f_0)$ were strongly correlated ($r = 0.868$, $R^2 = 0.754$), indicating substantial redundancy between the two site descriptors. A formulation containing simultaneous magnitude interactions for the two raw site descriptors showed substantial collinearity, with a maximum variance inflation factor (VIF) of 12.05, resulting in unstable interaction

estimates. When f_0 was introduced only as a main-effect control, the joint magnitude–Vs30 interaction remained essentially unchanged at 2.0 s ($p = 0.00343$) and 3.0 s ($p = 5.90 \times 10^{-7}$). The same result was obtained after residualizing f_0 with respect to Vs30, with joint interaction p-values of 0.00335 and 5.38×10^{-7}, respectively, whereas the magnitude interaction associated with the independent f_0 component was not significant at either period. These results indicate that the long-period magnitude-associated modulation is not explained solely by the independent component of the available fundamental-frequency proxy. Overall, the analyses identify a non-uniform spectral modulation of the Vs30 site term, motivating its scenario-dependent transfer to the digital soil field.

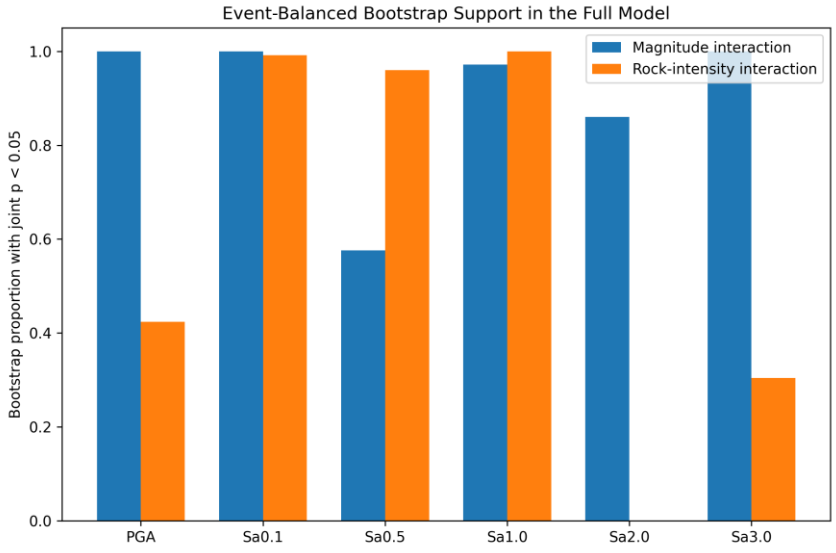

Figure 7. Event-balanced bootstrap support for magnitude- and reference-rock-intensity-dependent modulation of the Vs30 site term across PGA and spectral periods.

3.4. Amplification fields and propagated uncertainty

The observational amplification relationships were subsequently transferred to the SPT-derived digital Vs30 field. For the Mw ≥ 6.0 scenario, the central amplification factors range from 2.31 to 2.48 for PGA, from 2.59 to 2.82 at 1.0 s, from 2.78 to 3.04 at 2.0 s, and from 2.70 to 2.94 at 3.0 s. Representative spatial fields for PGA, Sa(1.0s), and Sa(3.0s) are shown in Figure 8.

The mapped amplification fields reproduce the broad spatial structure inherited from the digital Vs30 field, with larger amplification associated with lower Vs30 portions of the study area. The spatial contrasts are nevertheless modest relative to the total propagated uncertainty. For Mw ≥ 6.0, the full mapped PGA range corresponds to approximately 7.35% of the field-median amplification, compared with a median propagated 68% uncertainty of 11.69%. The corresponding values are 8.37% versus 13.65% at 1.0 s, 9.00% versus 13.26% at 2.0 s, and 8.74% versus 13.57% at 3.0 s.

The relationship between mapped spatial contrast and propagated uncertainty is shown explicitly in Figure 9. Across the principal intensity measures, the uncertainty envelope is comparable to or greater than the full within-field amplification contrast, indicating that the most

robust information lies in broad spatial tendencies and differences between seismic scenarios rather than in fine pixel-to-pixel variation.

The uncertainty comparison constrains the spatial resolution at which the amplification layers can be interpreted. The maps identify broad response gradients and scenario-dependent changes across the borehole-supported domain, but the available data do not support sharply bounded local amplification zones. This interpretation is consistent with the limited location-independent predictive performance of the underlying Vs30 interpolation. Uncertainty decomposition further showed that spatial prediction was the largest individual contributor to mapped amplification uncertainty. For the Mw ≥ 6.0 scenarios, the median relative uncertainty was approximately 8.35%–11.52% for spatial prediction, 4.07%–5.60% for SPT–Vs model-form variability, and 3.52%–6.51% for amplification-model uncertainty.

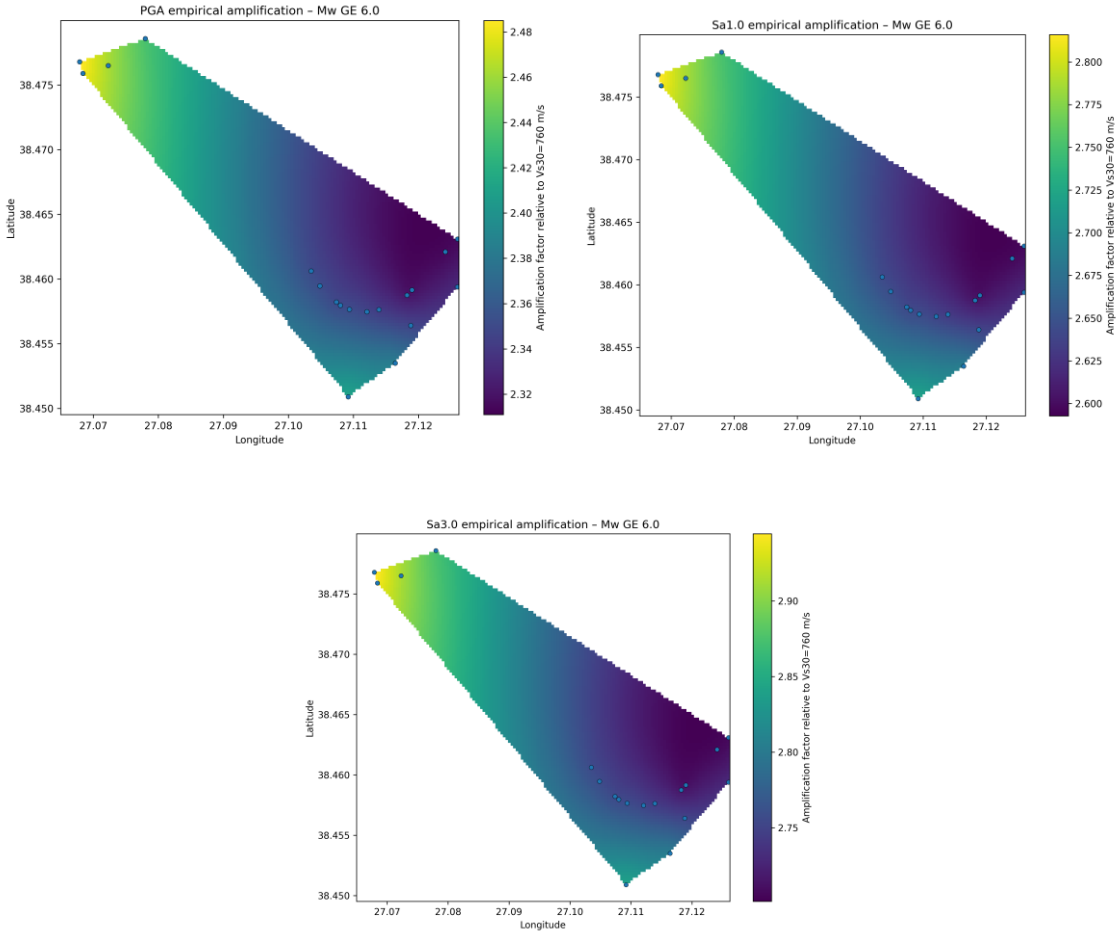

Figure 8. Representative scenario-dependent empirical amplification fields for the Mw ≥ 6.0 case: (a) PGA, (b) Sa(1.0s), and (c) Sa(3.0s).

A correlation-sensitivity analysis was also performed to examine how dependence among the uncertainty components affects the propagated response-field uncertainty. The analytic independent formulation reproduced the original Monte Carlo combined uncertainty closely, with a median absolute difference of 0.10% across scenarios. Introducing a moderate positive correlation of $\rho = 0.5$ increased the median propagated uncertainty by 30.77%, while perfect positive correlation between the SPT–Vs and spatial-prediction components produced a 31.87% increase. The all-perfect-positive case yielded the

largest increase, 55.74% relative to the independent baseline. For the Mw ≥ 6.0 scenarios, median relative uncertainty increased from approximately 10.40%–13.63% under independence to 14.07%–18.62%, 13.41%–17.57%, and 16.98%–22.59% for the three correlated cases, respectively.

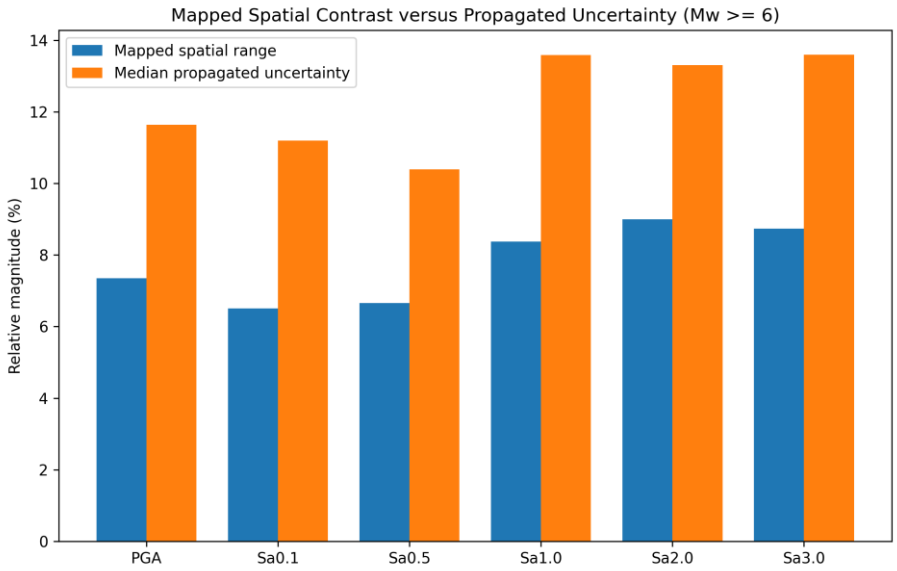

Figure 9. Relative magnitude of mapped spatial amplification contrast and propagated uncertainty for the Mw ≥ 6.0 scenario.

4. Discussion

The present study integrates borehole-based digital Vs30 mapping, observation-derived magnitude- and period-dependent site-amplification relationships, and explicit uncertainty propagation within a unified spatial framework. The ensemble SPT–Vs procedure provides the subsurface basis for a response-oriented formulation in which a single static soil field is expressed as multiple seismic-response states. Within this framework, the seismic expression of the mapped Vs30 field is conditioned by spectral period, earthquake magnitude, and input-motion characteristics, thereby extending static site characterization toward scenario-dependent response mapping.

4.1. Period-, magnitude-, and intensity-dependent site amplification

The inverse Vs30-amplification relationship is consistent with the established role of Vs30 as a first-order site-condition proxy and with empirical models in which softer sites exhibit stronger and period-dependent amplification [13]. The more distinctive result here is the non-uniform spectral structure of the modulation: magnitude-associated differences are pronounced for PGA and longer-period response but weaken around 0.5–1.0 s (Figure 5). This pattern remains after accounting for event and station dependence and is unchanged by station composition across magnitude groups. Overall, the Vs30–amplification relationship exhibits a non-uniform spectral organization, with stronger magnitude-associated modulation at PGA and longer periods and stronger spectral-intensity conditioning at intermediate periods.

The reference-rock analysis further indicates distinct spectral roles for earthquake magnitude and input-motion intensity. At intermediate periods, the corresponding spectral input amplitude contributes more strongly to the Vs30 site term, whereas magnitude-associated effects remain more persistent toward longer periods (Figure 6; Table 8). This behavior is consistent with frequency-dependent site response, as motion amplitude influences effective stiffness and damping while earthquake magnitude is associated with spectral content, duration, rupture characteristics, and energy distribution. Because the analysis is observational, the magnitude term is interpreted as magnitude-associated rather than directly causal.

The long-period sensitivity analysis provides an additional constraint on this interpretation. Station fundamental frequency f_0, used here as an available proxy for site-period and deeper-structure effects, was strongly correlated with Vs30, resulting in substantial collinearity when magnitude-dependent interactions for both descriptors were introduced simultaneously. When this redundancy was controlled either by including f_0 only as a main effect or by using the component of f_0 orthogonal to Vs30, the magnitude–Vs30 interaction at 2–3 s remained essentially unchanged, whereas the magnitude interaction associated with the independent f_0 component was not significant. The persistence of the magnitude–Vs30 interaction after controlling for f_0 shows that the available fundamental-frequency proxy does not account for the full long-period modulation. Direct deep-structure descriptors such as Z1.0, Z2.5, or measured deep velocity profiles would provide additional constraints on this interpretation.

4.2. What the SPT-derived Vs30 field represents

Vs30 captures a substantial component of repeatable seismic site response but remains a compact proxy for alluvial behavior. Sites with similar Vs30 may exhibit different spectral responses because of profile shape, deeper velocity structure, impedance contrasts, and fundamental site period [14]. In the present framework, Vs30 is derived from an ensemble of empirical SPT–Vs transformations, with the between-correlation spread retained as model-form uncertainty. The resulting field therefore represents shallow stiffness, while the mapped amplification layers describe its observation-conditioned seismic expression.

The independent SPAC comparison supports the regional plausibility of the adopted SPT–Vs ensemble. The agreement with the SPAC-derived shallow-velocity range for the İzmir Bay alluvial setting (S. Altun, unpublished technical assessment) provides an external geophysical consistency check, while the SPAC information is not used for calibration.

The empirical Vs30–amplification relationships were derived from a 34-station regional network and subsequently transferred to the compact urban alluvial domain represented by the SPT field. Geographic restriction of the strong-motion network preserved the characteristic spectral modulation pattern, with correlations of $r = 0.993$, 0.991, and 0.999 for the 25, 50, and 75 km subsets. The soft-site subset also retained the overall spectral pattern ($r = 0.970$), although absolute modulation ratios showed greater variation. These results indicate that the spectral organization of the response is comparatively stable across the tested subsets, while the absolute amplification level remains more sensitive to station population and local site conditions. The resulting layers therefore provide regionally conditioned scenario fields for screening and comparative assessment.

Alternative P25–P75 depth-prior completion strategies produced changes within the overall propagated uncertainty, supporting the selected completion method as a data-tested approximation whose influence is explicitly represented by the sensitivity analysis.

Residual station-specific variability confirms that Vs30 does not capture the full site-response signal, consistent with previous analyses of empirical station terms [19]. The framework therefore occupies an intermediate scale between geotechnical mapping and site-specific response analysis and is most appropriate for regional screening and scenario comparison. Site-specific applications would require complementary measured velocity profiles, fundamental-period estimates, deeper stratigraphic constraints, or direct site-response analyses.

4.3. Spatial predictability and effective map resolution

The contrast between strong profile-completion validation and much weaker location-independent spatial prediction indicates that interpolation between observation points is the larger source of predictive limitation (Table 4). The low predictive R^2 shows that a substantial fraction of borehole-scale variability is unresolved between locations; accordingly, the digital field represents broad stiffness tendencies at the spatial scale supported by the borehole network rather than fine-scale variability.

An additional auxiliary-covariate sensitivity analysis supports this interpretation. Groundwater depth, fines content, plasticity index, and spatial coordinates were introduced into several alternative prediction models and evaluated using the same strict leave-one-location-out framework. The best-performing auxiliary model, an Extra Trees regressor, reduced the RMSE from 28.59 to 27.13 m/s and increased predictive R^2 from 0.117 to 0.204, corresponding to only a 5.1% improvement in RMSE. The modest improvement obtained with the auxiliary models indicates that, within the variables evaluated here, spatial sampling density remains the main constraint on predictive resolution.

The propagated uncertainty supports the same interpretation. For the $Mw \geq 6.0$ scenarios, the within-field amplification contrast is generally smaller than the corresponding propagated uncertainty (Figure 9). The decomposition further shows that spatial prediction is the largest individual uncertainty source, contributing approximately 8.35%–11.52%, compared with about 4.07%–5.60% for SPT–Vs model-form variability and 3.52%–6.51% for amplification-model uncertainty.

Positive correlation among uncertainty components increased the propagated uncertainty, with the largest increase occurring under the all-perfect-positive upper-bound case. Nevertheless, the interpretation of the effective map resolution remained unchanged across the tested dependence structures.

4.4. Engineering implications and response-oriented digital soil mapping

The period dependence of the mapped response has practical implications for urban seismic assessment. PGA-based layers are relevant to acceleration-sensitive components and relatively stiff systems, whereas spectral acceleration at intermediate and longer periods provides a more direct descriptor for systems with corresponding dynamic characteristics. The results therefore support response-specific mapping rather than a single generic amplification layer.

The framework may also support evaluation of simplified code-based site factors by comparing discrete site classes and coefficients with observation-derived spectral trends. Given the spatial

uncertainty, such comparisons are most appropriately performed at the level of site-condition groups rather than individual grid cells.

The uncertainty decomposition also clarifies where future measurements would provide the greatest gain. Because prediction between boreholes dominates the spatial uncertainty, increasing the density and diversity of dynamic site observations is likely to be more effective than simply extending every borehole to greater depth. Distributed MASW surveys, downhole or PS logging, and ambient-vibration estimates of fundamental period could constrain variability between SPT locations and introduce dynamic descriptors not represented by a 30-m average velocity alone. These measurement priorities provide a direct pathway for improving the spatial resolution and site-specific applicability of future implementations.

5. Conclusions

This study developed a response-oriented digital soil-mapping framework in which depth-resolved SPT information was transformed into a borehole-based Vs30 proxy field, subsequently linked to empirical seismic amplification derived independently from regional strong-motion observations. The framework preserves the separation between subsurface characterization and seismic-response modeling until the final transfer stage, allowing uncertainty associated with the SPT–Vs transformation, spatial prediction, and amplification model to be propagated explicitly into the resulting response fields.

The SPT-based analysis showed that incomplete 20–30 m profiles could be incorporated with limited additional uncertainty when lower-profile treatment was selected through masked validation. Spatial prediction between boreholes was substantially less constrained than borehole-scale estimation, and uncertainty decomposition identified this interpolation step as the largest individual contributor to final amplification uncertainty. The resulting surface therefore resolves broad alluvial stiffness variability at the spatial scale supported by the borehole network.

Strong-motion observations revealed a persistent inverse relationship between Vs30 and empirical amplification across PGA and spectral periods from 0.1 to 3.0 s. The modulation of this relationship was strongly period-dependent and remained robust under event- and station-aware inference, bootstrap resampling, station-level analysis, and station-composition sensitivity tests. Magnitude-associated modulation was most persistent for PGA and longer-period response, whereas the intermediate-period range was more strongly conditioned by the corresponding spectral input-motion intensity. Earthquake magnitude and shaking amplitude therefore provide complementary rather than interchangeable descriptions of the observed site-response modulation.

These findings demonstrate that a digital Vs30 field does not correspond to a single seismic amplification field. The same mapped subsurface condition can acquire different engineering significance depending on spectral period, magnitude group, and input-motion condition. By converting a static borehole-derived soil representation into a family of observation-constrained, scenario-dependent response states, the framework extends digital soil mapping toward seismic-response interpretation. For urban alluvial areas where conventional borehole information is considerably denser than direct dynamic measurements, this provides a practical basis for regional

screening and scenario comparison, while future improvements would benefit most from spatially distributed dynamic measurements capable of constraining variability between boreholes.

Data availability

All data and models analyzed during the current study are available from the corresponding author on reasonable request.

Use of Generative-AI tools declaration

The author used ChatGPT (OpenAI) for language editing, manuscript organization, and assistance with computational workflow development. The author reviewed and verified all analyses, results, interpretations, references, and final text and takes full responsibility for the content of the article.

Acknowledgments

This research was supported by Yaşar University Scientific Research Project (BAP) Program (Project No. BAP148), titled "Application of Artificial Intelligence to Enhance Seismic Hazard Maps and Risk Mitigation Strategies in Izmir".

Conflict of interest

The authors declare that they have no known competing financial interests or personal relationships that could have appeared to influence the work reported in this paper.

References

1. Borcherdt RD (2012) VS30—A site-characterization parameter for use in building codes, simplified earthquake resistant design, GMPEs, and ShakeMaps, *Proceedings of the 15th World Conference on Earthquake Engineering*, Lisbon, Portugal.
2. Boore DM, Stewart JP, Seyhan E, et al. (2014) NGA-West2 equations for predicting PGA, PGV, and 5% damped PSA for shallow crustal earthquakes. *Earthq Spectra* 30: 1057–1085. https://doi.org/10.1193/070113EQS184M
3. Tinsley JC, Hough SE, Yong AK, et al. (2004) Geotechnical characterization of TriNet sites: A status report. *Seismol Res Lett* 75: 505–514. https://doi.org/10.1785/gssrl.75.4.505
4. Aki K (1993) Local site effects on weak and strong ground motion. *Tectonophysics* 218: 93–111. https://doi.org/10.1016/0040-1951(93)90262-I
5. McBratney AB, Mendonça Santos ML, Minasny B (2003) On digital soil mapping. *Geoderma* 117: 3–52. https://doi.org/10.1016/S0016-7061(03)00223-4
6. Abbasnejadfard M, Bastami M, Jafari MK, et al. (2023) Spatial correlation models of V_{S30} values: A case study of the Tehran region. *Eng Geol* 325: 107300. https://doi.org/10.1016/j.enggeo.2023.107300

7. Aas A, Sinha SK (2023) Seismic site characterization using MASW and correlation study between shear wave velocity and SPT-N. *J Appl Geophys* 215: 105131. https://doi.org/10.1016/j.jappgeo.2023.105131
8. Ohta Y, Goto N (1978) Empirical shear wave velocity equations in terms of characteristic soil indexes. *Earthquake Engng Struct Dyn* 6: 167–187. https://doi.org/10.1002/eqe.4290060205
9. Hasancebi N, Ulusay R (2007) Empirical correlations between shear wave velocity and penetration resistance for ground shaking assessments. *Bull Eng Geol Environ* 66: 203–213. https://doi.org/10.1007/s10064-006-0063-0
10. Dikmen Ü (2009) Statistical correlations of shear wave velocity and penetration resistance for soils. *J Geophys Eng* 6: 61–72. https://doi.org/10.1088/1742-2132/6/1/007
11. Kuo CH, Wen KL, Hsieh HH, et al. (2011) Evaluating empirical regression equations for Vs and estimating Vs30 in northeastern Taiwan. *Soil Dyn Earthq Eng* 31: 431–439. https://doi.org/10.1016/j.soildyn.2010.09.012
12. Chiou BSJ, Youngs RR (2014) Update of the Chiou and Youngs NGA model for the average horizontal component of peak ground motion and response spectra. *Earthq Spectra* 30: 1117–1153. https://doi.org/10.1193/072813EQS219M
13. Seyhan E, Stewart JP (2014) Semi-empirical nonlinear site amplification from NGA-West2 data and simulations. *Earthq Spectra* 30: 1241–1256. https://doi.org/10.1193/063013EQS181M
14. Derras B, Bard PY, Régnier J, et al. (2020) Non-linear modulation of site response: Sensitivity to various surface ground-motion intensity measures and site-condition proxies using a neural network approach. *Eng Geol* 269: 105500. https://doi.org/10.1016/j.enggeo.2020.105500
15. Özmen OT, Yamanaka H, Arslan HI, et al. (2026) Site amplification estimated from strong motion records at Türkiye strong-motion stations using spectral separation technique. *Soil Dyn Earthq Eng* 207: 110350. https://doi.org/10.1016/j.soildyn.2026.110350
16. Disaster and Emergency Management Authority, Turkish National Strong Motion Network [Data set]. International Federation of Digital Seismograph Networks. 1973. https://doi.org/10.7914/SN/TK
17. Imai T, Yoshimura Y (1970) Elastic Wave Velocity and Soil Properties in Soft Soil. Tsuchi-ToKiso, 18: 17–22. In Japanese.
18. Imai T, Tonouchi K (1982) Correlation of N-value with S-wave velocity and shear modulus. *Proceedings of the 2nd European Symposium on Penetration Testing*, A. A. Balkema, 67–72.
19. Thompson EM, Wald DJ (2016) Uncertainty in VS30-based site response. *Bull Seismol Soc Am* 106: 453–463. https://doi.org/10.1785/0120150214



© 2026 the Author(s), licensee AIMS Press. This is an open access article distributed under the terms of the Creative Commons Attribution License (https://creativecommons.org/licenses/by/4.0)